Letter

Analysis of High-Performing Terahertz Quantum Cascade Lasers

Viktor Rindert, Ekin Önder, and Andreas Wacker*
Mathematical Physics and NanoLund, Lund University, Box 118, Lund 22100, Sweden

(Received 16 June 2022; revised 15 August 2022; accepted 15 September 2022; published 21 October 2022)

Detailed simulations for terahertz quantum cascade lasers based on two-well designs are presented. We reproduce the maximal operation temperatures observed and attribute the degradation with temperature to the occupation of parasitic levels and thermal backfilling. Furthermore, we demonstrate that the current injection can be conveniently studied by using states, which combine energy selectivity and spatial localization. Improving the injection allows achievement of higher maximal operation temperatures around 265 K.

DOI: 10.1103/PhysRevApplied.18.L041001

The quantum cascade laser (QCL) [1] is one of the most relevant devices for IR radiation, in particular, since room-temperature operation could be achieved [2]. This is still a main goal for QCLs operating in the terahertz (THz) region [3] (i.e., below the optical phonon frequency). While there had been no improvement for a long time after scratching the 200-K mark in 2012 [4], recently a significant improvement was achieved based on two-well designs resulting in thermoelectrically cooled [5] and portable [6] systems operating up to 250 K. More information on the different design ideas and their benefits can be found in the recent review [7].

In this work, we focus on two-well designs, where essentially three levels are of relevance. Next to the upper (u) and lower (l) laser level, the ground (g) level extracts electrons from the lower level by phonon emission and injects them into the upper level of the subsequent module by resonant tunneling. This is the minimal design for any QCL [8–10] and has thus the benefit of a rather simple and robust design allowing for short modules with high gain per length. Upon increasing the doping density and barrier height following detailed simulations, these structures became superior to other designs [5,11]. Using even higher barriers, the current record operational temperature of 250 K was reported in 2021 [6].

In Ref. [6] it was argued that the key benefit of their design is the establishment of a pure three-level design, where other levels are carefully separated in energy and space. This also reduces leakage, an issue for devices with a short module length [12–16]. In this letter we want to investigate this point for the structures with highest operation temperature. We show that the increased energy separation between the lower laser and ground level plays a role, which reduces the thermal backfilling as already suggested in Refs. [17–19]. Furthermore, we analyze the injection in detail. Based on these considerations, we propose a structure, named LU2022, which according to our modeling operates at even higher temperatures.

The calculations presented here are based on our nonequilibrium Green's function (NEGF) code, detailed in Ref. [20]. Unless mentioned otherwise all parameters used in this work are given in Ref. [21], where the versatility and accuracy of the model is detailed. We use seven levels per module [22] and repeat the modules 2 times in each direction in the simulations in order to allow for tunneling over more than one module boundary and the population of higher parasitic states (indexed by p). We note that the temperature used in the calculations mainly [23] determines the thermal occupation of the phonon modes and is referred to as phonon temperature T_{ph} in the following.

We assume total losses of 20/cm for the metal-metal waveguides used in Refs. [5,6] around 4 THz. This is consistent with data from Ref. [24] and was also used in Ref. [21].

It was noted earlier [21], that our NEGF code systematically produced higher currents than observed for samples reported from the MIT group, when using our standard conduction-band offset $\Delta E_c^1 = x \times 0.831$ eV [25] for $Al_xGa_{1-x}As$ barriers. In contrast much better agreement in currents was found for samples from the ETH group. In this respect it is interesting to note, that both groups internally use different band offsets, when they show band diagrams. The ETH group [5] uses values that are consistent with ΔE_c^1. In contrast, a higher value is used by the MIT group. From the figures and the

*Andreas.Wacker@teorfys.lu.se

supplementary information of Ref. [6] we extract $\Delta E_c^2 = x \times 1.01$ eV based on the $Al_xGa_{1-x}As$ band gap reported in Ref. [26] together with a phenomenological 72% share of the conduction-band offset.

Table I provides simulation results for threshold and peak currents (under lasing conditions where gain matches the losses) for the QCL devices of Refs. [5,6]. We find good quantitative agreement if ΔE_c^2 is applied for the MIT devices. On the other hand, ΔE_c^1 is slightly better (albeit possibly too small) for the ETH device. We do not have an explanation for this difference, which is consistent with the observations in Ref. [21]. A straightforward explanation could be that the Al-content x is calibrated differently in both labs. On the other hand, the geometrical definition of barriers might be different. Furthermore, a part of the difference, may be attributed to the nonlinear behavior of ΔE_c in x, as the ETH device as a lower Al content. In the following we use ΔE_c^1 for the ETH sample of Ref. [5] and ΔE_c^2 for the MIT samples of Ref. [6], i.e., we use the values given by the respective groups.

In Fig. 1, we show the maximum gain (without lasing) obtained for different samples as a function of the phonon temperature. We find that the device ETH2019 [5] shows higher gain at low temperatures but gain is dropping stronger with temperature compared to the MIT devices [6]. The condition that gain needs to compensate for losses allows us to determine the maximum phonon temperature for operation. In the inset of Fig. 1 the crosses indicate the observed maximal heatsink operation temperatures. These agree well with the calculated maximal gain under the assumption, that the phonon temperature is 90 K larger than the heatsink temperature reported in the experimental work. While we did not perform simulations on the phonon kinetics, we note that the order of magnitude of this shift is consistent with more detailed studies [27,28]. This holds in particular for the most relevant optical phonons, which are expected to become quickly excited even for short pulses. Thus our simulations provide a good description for the differences in maximal lasing temperature of the samples.

TABLE I. Experimental and simulation results using different band offsets $\Delta E_c^{1/2}$ for the devices ETH2019 from Ref. [5] and MITG552/652 from Ref. [6]. The simulations are performed for $T_{ph} = 100$ K and the experimental values are extracted for the lowest temperature displayed.

Wafer	ETH2019	MITG552	MITG652
J_{max}^{exp} (kA/cm^2)	3.5	2.67	2.6
J_{max}^{sim} (kA/cm^2) for ΔE_c^1	4.3	3.3	3.6
J_{max}^{sim} (kA/cm^2) for ΔE_c^2	2.8	2.5	2.7
J_{th}^{exp} (kA/cm^2)	2	1.48	1.54
J_{th}^{sim} (kA/cm^2) for ΔE_c^1	2.6	1.9	2.4
J_{th}^{sim} (kA/cm^2) for ΔE_c^2	1.4	1.2	1.4

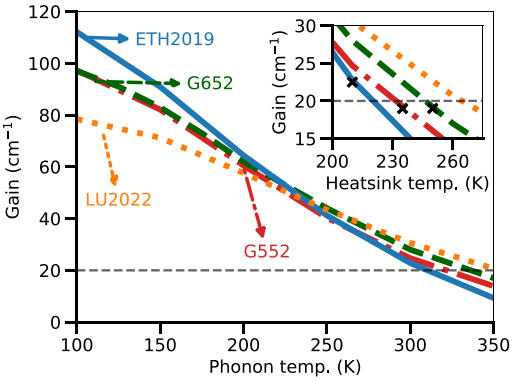

FIG. 1. Maximal gain as a function of phonon temperature for the samples from Refs. [5,6] and the design LU2022 suggested here. The peak gain is evaluated at the maximal current (without lasing) for the given temperature. The inset shows the same data for temperatures reduced by 90 K, which is our estimate for the difference between heatsink and phonon temperature. The crosses indicate the maximal heatsink temperature, where laser operation is observed experimentally.

In Fig. 1 we add an additional design, called LU2022, which shows even better temperature stability. From the intersection of the peak gain with the expected losses of 20/cm in the inset, we expect a maximal operation temperature around 265 K. Details on this design are given in Fig. 2. We note that the current densities are comparable to the MIT devices and lower than the ETH device, which demonstrates that the device is manageable in existing setups. In these calculations we use the band offset ΔE_c^2, as appropriate for MIT samples. Applying instead ΔE_c^1, we get almost identical results for an increased Al concentration $x = 0.35$. This indicates that an x value slightly above 0.3 might be appropriate for other labs.

In order to analyze the temperature dependence, we extract the occupations of the levels as a function of temperature for the bias with maximal gain. These are displayed in Fig. 3, where we add the expression

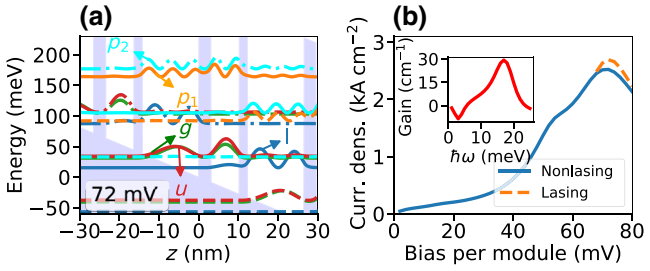

FIG. 2. The proposed device LU2022 with a layer sequence **31**/71/**21**/142 (in Å with $x = 0.3$ barriers in bold face), where the central 3 nm of the largest well are n doped with 4.5×10^{10} cm^{-2} per module. Left: band diagram at peak current. Right: current bias relation for $T_{ph} = 300$ K. The inset shows the gain spectrum at the current peak without lasing.

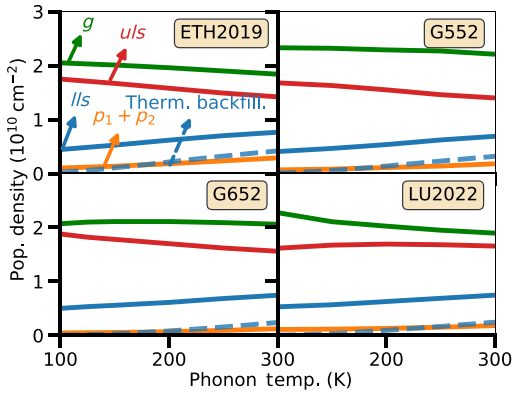

FIG. 3. Calculated occupation of the energy eigenstates (full lines) and estimated contribution from thermal back-filling for the lower laser level (dashed line) for different samples.

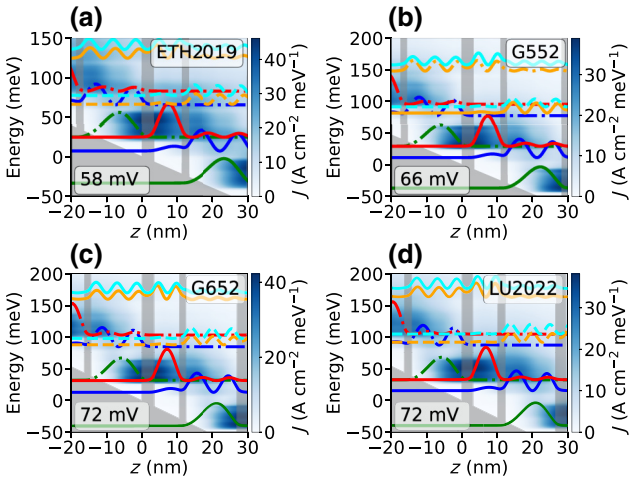

FIG. 4. Calculated current distribution for different samples at peak bias and a phonon temperature of 350 K together with the EZ states defined in the text below.

$n_g \; e^{-(E_l - E_g)/k_B T_{\rm ph}}$ due to thermal backfilling from the ground level g. We find that thermal backfilling provides the essential ingredient in the thermal increase in population of the lower laser level. Here the sample ETH2019 has a level separation $E_l - E_g = 38$ meV at the peak gain. This approximately equals the longitudinal optical phonon energy and provides the quickest emptying for the lower laser level [29] and is traditionally used in QCL designs. In contrast, the samples MITG552, MITG652, LU2022 exhibit a significantly larger separation of 47, 53, and 53 meV, respectively, which reduces thermal backfilling. We suggest that this can relate to the better temperature stability visible in Fig. 1. This had been already addressed in Ref. [18] for two-well designs and is actually the same scenario as observed for infrared QCLs, where the reduction of thermal backfilling due to double-phonon extraction allowed for room-temperature operation [2]. On the other hand, ETH2019 has the highest gain at low phonon temperatures, showing that it is actually the better design here.

Reference [6] stated that a pure three-level design should be favored as this prevents electrons escaping. Figure 3 shows that the ETH sample has indeed a larger occupation of the parasitic levels (denoted as $p1$ and $p2$ here) at high temperature compared to the top-performing devices MITG652 and LU2022. This can also be seen in the spatioenergetically resolved current densities in Fig. 4, where higher states contribute more for the ETH sample. In all cases the levels $p1$ and $p2$ are energetically close to the lower and upper laser level. Thus the key mechanism is the use of higher barriers reducing resonant currents and the larger vertical energy separation, reducing excitations from the u, l, g levels into the parasitic states.

The decrease of gain with temperature (see Fig. 1) is much stronger than one would expect based on the decrease in inversion $n_u - n_l$ as calculated by the common energy eigenstates (see Fig. 3). In Ref. [30] such a difference was related to the scattering rates increasing with temperature, which result in a stronger broadening of the gain spectrum. For the data presented here, we also see this trend, but it is by far not strong enough to provide the substantial decrease in gain.

It is well known [31,32] that the energy eigenstates as, e.g., shown in Figs. 2(a) and 5(c) are not a good basis if the energy separation is smaller than the broadening. In this case, the coherences between the states must be carefully taken into account. Here we achieve this by identifying multiplets of energy eigenstates $|\Psi_j\rangle$, which are close in energy. (Specifically, we add a state to a multiplet if its energy differs by less than 5 meV to at least one other member of the multiplet.) Restricting the general expression for the spatial electron density $n(z)$ to the states of the multiplet, we get

$$n_{\rm multiplet}(z) = \sum_{i,j \in {\rm multiplet}} \rho_{ij} \, \Psi_j^*(z) \Psi_i(z), \qquad (1)$$

where $\Psi_i(z)$ are the wave functions of the states. ρ_{ij} is the density matrix within this basis, where the diagonal elements provide the occupations of the states (in $1/{\rm cm}^2$) and the nondiagonal elements (also called polarizations) shift the electron density in space. Results are shown in the upper panels of Fig. 5 for the devices MITG652 (a) and LU2022 (b). In both cases, the electrons mostly stay on the left side of the injection barrier around $z = 0$ (red full line). This is not well reflected by the sum of densities of the energy eigenstates (red dotted line), where the occupations of the upper laser state and the ground state are pretty similar at resonance, see Fig. 3. Furthermore, we note, that the injection to the right side of the barrier, from where optical transitions to the lower laser level occur, is better

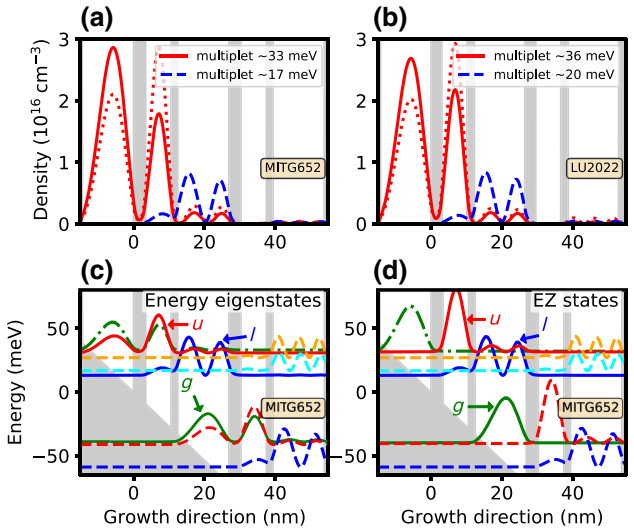

FIG. 5. Upper panels: electron density from Eq. (1) for the multiplet including the upper laser level (red full) and the multiplet including the lower laser level (blue dashed) for the sample MITG652 (a) and LU2022 (b). The red dotted line restricts to the diagonal elements of ρ_{ij} for the upper level multiplet. Lower panels: absolute square of wave functions for the sample MITG652. (c) Energy eigenstates; (d) EZ states. All data is extracted from our NEGF simulations at $T_{\mathrm{ph}} = 350$ K at the peak bias of 72 mV/module.

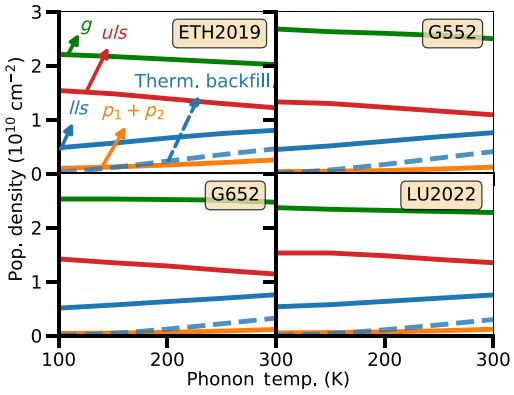

FIG. 6. Calculated occupations of the EZ states (full lines) and estimated contribution from thermal backfilling for the lower laser level (dashed line) for different samples.

for LU2022, which has a slightly thinner injection barrier. This appears the key point for the better performance of LU2022 at high temperatures.

In order to quantify the injection, it is better to use a localized basis. For this purpose we calculate the matrix $\langle \Psi_i | \hat{z} | \Psi_j \rangle$ for each multiplet. Diagonalizing this matrix provides the basis transformation from the energy eigenstates of each multiplet to localized states, which we call EZ states in the following. (The name is motivated by the reasonably well-defined energy E and position z within the subspace of the multiplet.) In the lower panels of Fig. 5, we show a comparison between the energy eigenstates (c) and the EZ states (d), showing that the ground (green) and upper laser level (red) are much better defined for the EZ states. In contrast, the corresponding energy eigenstates represent binding and antibinding combinations, where the absolute square of the wave function is very similar at resonance. By construction these EZ states provide an orthonormal basis, where the diagonal elements of the Hamiltonian (transformed into this basis) provide the energy of the states and nondiagonal elements represent tunnel couplings Ω between almost degenerate states within a multiplet.

Figure 6 shows the occupations of the EZ states (obtained from the diagonal elements of the density matrix transformed to EZ states). Here the occupations of the upper laser level are significantly lower than the occupations of the ground level. Furthermore, the difference between the upper and lower laser levels decreases drastically with temperature, explaining the major part of the temperature drop in gain.

Considering the EZ states in Fig. 6, the difference between the ground and upper laser level hardly changes with temperature for all devices. This difference is actually proportional to the injection current in the device, which has no strong temperature dependence at the current peak, see also Ref. [33]. For sequential tunneling, where the broadening Γ surpasses the tunnel coupling Ω, we find similar to Eq. (83) of Ref. [34]

$$J_{i\to u}^{\text{seq. tunnel.}} = \frac{e\Omega^2}{\hbar} \frac{\Gamma}{(E_u - E_i)^2 + \Gamma^2/4} (n_i - n_u), \quad (2)$$

which provides very good agreement for all samples with $\Gamma \sim 6$–8 meV. Here we extract $\Omega = 1.58$, 1.08, 1.17, and 1.49 meV for the samples ETH2019, MITG552, MITG652, and LU2022, respectively, from the Hamiltonian transferred to the EZ basis. (The values for the MIT samples agree very well with the anticrossing gaps Ω_{iu} reported in Table 1 of Ref. [6], which correspond to 2Ω in our notation.) The rather low value of Ω explains the large differences between n_u and n_i for the MIT samples. This actually limits the inversion, as it provides an upper bound for n_u. In contrast our design LU2022 has a thinner injection barrier, while it restricts the current by a larger lasing barrier, which results in better behavior. On the other hand, for ETH2019 the injection in more efficient (even if it is taken into account that the currents are higher). Here the limiting factor is the higher thermal backfilling and the population of enhanced higher states addressed above.

Conclusion: Using NEGF simulations, we can quantitatively reproduce the observed maximal operation temperatures of high-performing three-level designs. We confirm that the occupation of higher states with increasing temperature and thermal backfilling is detrimental for the design of Ref. [5]. Both issues are improved in the MIT

designs [6] using higher barriers. However, these MIT designs have a rather thick injector barrier leading to a significant difference between the occupations of the ground and upper laser state, which limits inversion. This issue can be conveniently analyzed by using EZ states. These are obtained from the energy eigenstates (E), which are sorted to multiplets with similar energy. Then the Z operator is diagonalized within each multiplet subspace, providing the EZ states. The analysis shows that the devices of Ref. [6] suffer from insufficient injection. Using a thinner injection barrier while limiting the current increase by a thicker radiation barrier, we can identify a design, which is estimated to operate up to 265 K.

ACKNOWLEDGMENTS

We thank the Swedish Research Council (project 2017-04287_VR) and NanoLund for financial support.

[1] J. Faist, F. Capasso, D. L. Sivco, C. Sirtori, A. L. Hutchinson, and A. Y. Cho, Quantum cascade laser, Science **264**, 553 (1994).
[2] M. Beck, D. Hofstetter, T. Aellen, J. Faist, U. Oesterle, M. Ilegems, E. Gini, and H. Melchior, Continuous wave operation of a mid-infrared semiconductor laser at room temperature, Science **295**, 301 (2002).
[3] R. Köhler, A. Tredicucci, F. Beltram, H. E. Beere, E. H. Linfield, A. G. Davies, D. A. Ritchie, R. C. Iotti, and F. Rossi, Terahertz semiconductor-heterostructure laser, Nature **417**, 156 (2002).
[4] S. Fathololoumi, E. Dupont, C. Chan, Z. Wasilewski, S. Laframboise, D. Ban, A. Mátyás, C. Jirauschek, Q. Hu, and H. C. Liu, Terahertz quantum cascade lasers operating up to $\sim$ 200 K with optimized oscillator strength and improved injection tunneling, Opt. Express **20**, 3866 (2012).
[5] L. Bosco, M. Franckié, G. Scalari, M. Beck, A. Wacker, and J. Faist, Thermoelectrically cooled THz quantum cascade laser operating up to 210 K, Appl. Phys. Lett. **115**, 010601 (2019).
[6] A. Khalatpour, A. K. Paulsen, C. Deimert, Z. R. Wasilewski, and Q. Hu, High-power portable terahertz laser systems, Nat. Photonics **15**, 16 (2021).
[7] B. Wen and D. Ban, High-temperature terahertz quantum cascade lasers, Prog. Quantum Electron. **80**, 100363 (2021).
[8] S. Kumar, C. W. I. Chan, Q. Hu, and J. L. Reno, Two-well terahertz quantum-cascade laser with direct intrawell-phonon depopulation, Appl. Phys. Lett. **95**, 141110 (2009).
[9] G. Scalari, M. I. Amanti, C. Walther, R. Terazzi, M. Beck, and J. Faist, Broadband THz lasing from a photon-phonon quantum cascade structure, Opt. Express **18**, 8043 (2010).
[10] A. Wacker, Extraction-controlled quantum cascade lasers, Appl. Phys. Lett. **97**, 081105 (2010).
[11] M. Franckié, L. Bosco, M. Beck, C. Bonzon, E. Mavrona, G. Scalari, A. Wacker, and J. Faist, Two-well quantum cascade laser optimization by non-equilibrium Green's function modelling, Appl. Phys. Lett. **112**, 021104 (2018).
[12] S. Khanal, L. Zhao, J. L. Reno, and S. Kumar, Temperature performance of terahertz quantum-cascade lasers with resonant-phonon active-regions, J. Opt. **16**, 094001 (2014).
[13] A. Albo and Q. Hu, Carrier leakage into the continuum in diagonal GaAs/$Al_{0.15}$GaAs terahertz quantum cascade lasers, Appl. Phys. Lett. **107**, 241101 (2015).
[14] A. Albo, Y. V. Flores, Q. Hu, and J. L. Reno, Two-well terahertz quantum cascade lasers with suppressed carrier leakage, Appl. Phys. Lett. **111**, 111107 (2017).
[15] L. Wang, T. Lin, M. Chen, K. Wang, and H. Hirayama, Leakages suppression by isolating the desired quantum levels for high-temperature terahertz quantum cascade lasers, Sci. Rep. **11**, 23634 (2021).
[16] T. Miyoshi and D. Ban, Barrier height study of two-well resonant-phonon terahertz quantum cascade lasers. I. The third-order tunneling current theory, J. Appl. Phys. **130**, 183103 (2021).
[17] A. N. Baranov, H. Nguyen-Van, Z. Loghmari, M. Bahriz, and R. Teissier, Terahertz quantum cascade laser with non-resonant extraction, AIP Adv. **9**, 055214 (2019).
[18] M. Franckié and J. Faist, Bayesian Optimization of Terahertz Quantum Cascade Lasers, Phys. Rev. Appl. **13**, 034025 (2020).
[19] A. Demić, Z. Ikonić, P. Dean, and D. Indjin, Prospects of temperature performance enhancement through higher resonant phonon transition designs in GaAs-based terahertz quantum-cascade lasers, New J. Phys. **24**, 033047 (2022).
[20] A. Wacker, M. Lindskog, and D. O. Winge, Nonequilibrium Green's function model for simulation of quantum cascade laser devices under operating conditions, IEEE J. Sel. Top. Quantum **19**, 1200611 (2013).
[21] D. O. Winge, M. Franckié, and A. Wacker, Simulating terahertz quantum cascade lasers: Trends from samples from different labs, J. Appl. Phys. **120**, 114302 (2016).
[22] This includes all Wannier levels below ΔE_c and at least one level above ΔE_c for all samples, so that all possible tunneling events among bound states are safely included.
[23] It also enters the screening of the potential from ionized impurities.
[24] Y. J. Han, L. H. Li, J. Zhu, A. Valavanis, J. R. Freeman, L. Chen, M. Rosamond, P. Dean, A. G. Davies, and E. H. Linfield, Silver-based surface plasmon waveguide for terahertz quantum cascade lasers, Opt. Express **26**, 3814 (2018).
[25] W. Yi, V. Narayanamurti, H. Lu, M. A. Scarpulla, and A. C. Gossard, Probing semiconductor band structures and heterojunction interface properties with ballistic carrier emission: GaAs/Al_xGa_{1-x}As as a model system, Phys. Rev. B **81**, 235325 (2010).
[26] Z. R. Wasilewski, M. M. Dion, D. J. Lockwood, P. Poole, R. W. Streater, and A. J. SpringThorpe, Composition of AlGaAs, J. Appl. Phys. **81**, 1683 (1997).
[27] M. S. Vitiello, R. C. Iotti, F. Rossi, L. Mahler, A. Tredicucci, H. E. Beere, D. A. Ritchie, Q. Hu, and G. Scamarcio, Non-equilibrium longitudinal and transverse optical phonons in terahertz quantum cascade lasers, Appl. Phys. Lett. **100**, 091101 (2012).
[28] Y. B. Shi and I. Knezevic, Nonequilibrium phonon effects in midinfrared quantum cascade lasers, J. Appl. Phys. **116**, 123105 (2014).

[29] R. Ferreira and G. Bastard, Evaluation of some scattering times for electrons in unbiased and biased single- and multiple-quantum-well structures, Phys. Rev. B **40**, 1074 (1989).

[30] R. Nelander and A. Wacker, Temperature dependence of the gain profile for terahertz quantum cascade lasers, Appl. Phys. Lett. **92**, 081102 (2008).

[31] H. Callebaut and Q. Hu, Importance of coherence for electron transport in terahertz quantum cascade lasers, J. Appl. Phys. **98**, 104505 (2005).

[32] A. Wacker and A.-P. Jauho, Quantum Transport: The Link between Standard Approaches in Superlattices, Phys. Rev. Lett. **80**, 369 (1998).

[33] W. Freeman, Longitudinal-optical phonon absorption and dephasing in three-level terahertz quantum cascade structures with different injector anticrossings, J. Appl. Phys. **128**, 235702 (2020).

[34] A. Wacker, Semiconductor superlattices: A model system for nonlinear transport, Phys. Rep. **357**, 1 (2002).